# Supplementary Information

# Geometrically Stabilized Skyrmionic Vortex in FeGe Tetrahedral Nanoparticles

**Authors:** K. Niitsu[1,2*,†], Y. Liu[1†], A. C. Booth[3], X. Z. Yu[1], N. Mathur[4], M. J. Stolt[4], D. Shindo[1] , S. Jin[4], J. Zang[3*], N. Nagaosa[1,5], Y. Tokura[1,5,6]

**Affiliations:**

[1]RIKEN Center for Emergent Matter Science (CEMS), Wako, Japan.

[2]Department of Materials Science and Engineering, Kyoto University, Sakyo-ku, Japan.

[3]Department of Physics and Astronomy, University of New Hampshire, Durham, NH, USA.

[4]Department of Chemistry, University of Wisconsin-Madison, Madison, WI, USA.

[5]Department of Applied Physics, University of Tokyo, Bunkyo-ku, Japan.

[6]Tokyo College, University of Tokyo, Bunkyo-ku, Japan.

†Equal contribution

*Correspondence to: niitsu.koudai.8z@kyoto-u.ac.jp and Jiadong.Zang@unh.edu

**This file includes:**

1. Supplementary Note 1: **Topological charge calculation of the skyrmionic vortex state**
2. Supplementary Note 2: **Energy landscape of magnetic states in FeGe tetrahedral nanoparticles**
3. Supplementary Figure 1 to 7
4. Captions of Supplementary Movies 1 to 2

**Other Supplementary Information for this manuscript include the following:**

Supplementary Movies 1 to 2

## Supplementary Note 1: Topological charge calculation of the skyrmionic vortex state

The magnetic configuration formed in a 145-nm tetrahedron is shown in Fig. 2 of the main text and in Supplementary Fig. 6. As observed in Supplementary Fig. 6a, the equi-spin surface for all spins with $S_z = 0$ ($z$-axis along the $[001]$ direction) forms a potbelly-shaped tube along the $z$-direction. The tube ends at two opposite edges of the tetrahedron. Therefore, the topological charge is computed for the $[001]$ projection of the magnetic configuration (achieved by first averaging the magnetization along the $z$-axis and then renormalizing the magnetization unit vector), whose magnetic configuration is shown in Supplementary Fig. 6b, and the corresponding topological charge density $\rho_Q = \hat{S} \cdot (\partial_x \hat{S} \times \partial_y \hat{S})/4\pi$ is shown in Supplementary Fig. 6c. Enclosed by the dashed line, the magnetic configuration resembles a skyrmionic texture, and the topological charge adds up to 0.93. Although a fractional number, it is very close to 1 for a perfect skyrmion. In finite geometries, the real-space manifold is not compact, and topological indices allow fractional values. The deviation is also attributed to the entanglement of the skyrmion texture and the corner spin twists outside the box. Actually, the topological charge $Q = m \cdot \Delta S_z/2$, where $m$ is the vorticity in the skyrmion plane and $\Delta S_z$ is the difference in the $z$-component of the magnetizations of the center and periphery. In this sense, the spin texture inside the box resembles key features of a skyrmion: it has unity vorticity because in-plane magnetic moments rotate by an angle of $2\pi$ circulating around the center, magnetic moments therein flip their $z$-components from the center to the periphery, and in 3D, it forms countable tubes. In light of its similarity to a skyrmion and to fully account for the fractional topological charge, we dubbed this state as a *skyrmionic vortex* to distinguish it from a perfect skyrmion.

## Supplementary Note 2: Energy landscape of magnetic states in FeGe tetrahedral nanoparticles

When the surface-to-volume ratio is small, tetrahedral nanoparticles are expected to host the bulk-like ground state, i.e., helical state, in which the helix direction is determined by the detailed magnetic interaction and the size of the tetrahedron. As the surface to volume ratio increases, surface effects (e.g., additional symmetry breaking at the surface of the tetrahedron) and geometrical confinement play vital roles, which lead to more complicated energy landscapes and give rise to the formation of rich magnetic states. These different magnetic states will be discussed in detail below.

### 1. Transition of helix directions

In both the experiments and simulations, a transition of the helix direction occurred when the tetrahedron size was approximately 300 nm. To understand the phase diagram, we can first analyze this transition of the helix direction from $[111]$ (or its equivalence, Supplementary Fig. 7a) to $[001]$ (or its equivalence, Supplementary Fig. 7b). The magnetic energy under consideration is given by

$$H = H_{\text{ex}} + H_{\text{cubic}} + H_{\text{surf}} + H_d$$

where $H_{\text{ex}} = \int d^3r \;\; [J(\nabla \boldsymbol{M})^2 + D\boldsymbol{M} \cdot (\nabla \times \boldsymbol{M})]$ includes ferromagnetic exchange and the DM interaction. $H_{\text{cubic}} = K_c \int d^3r \;\; (M_x^4 + M_y^4 + M_z^4)$ is the cubic crystalline anisotropy. $H_{\text{surf}} = K_s \int d\sigma(\boldsymbol{M} \cdot \hat{n})^2$ is the surface anisotropy associated with four surfaces of the tetrahedron. $\hat{n}$ is the normal direction of each surface. The last term $H_d$ is the dipolar energy. Magnetization in any helix can be expressed as

$$\boldsymbol{M} = (M_s/2)[\boldsymbol{m_q} \exp(-i(\boldsymbol{q} \cdot \boldsymbol{r} + \theta)) + c.c.],$$

where $\boldsymbol{q}$ is the wavevector, $M_s$ is the saturation magnetization, and $\theta$ is the phase shift. Equivalently, $\boldsymbol{M}/M_s = \Re(\boldsymbol{m_q}) \cos(\boldsymbol{q} \cdot \boldsymbol{r} + \theta) + \Im(\boldsymbol{m_q}) \sin(\boldsymbol{q} \cdot \boldsymbol{r} + \theta)$. For the $[111]$ helix, $\boldsymbol{q} = (111)q/\sqrt{3}$, and we chose $\boldsymbol{m_q} = \frac{1}{\sqrt{2}}(10\bar{1}) + \frac{i}{\sqrt{6}}(\bar{1}2\bar{1})$. For $[001]$ helix, $\boldsymbol{q} = (001)q$, and $\boldsymbol{m_q} = (100) + i(010)$. The geometry is shown in Supplementary Fig. 7c. For simplicity, we select the cubic size $a$ as our length scale, such that the edge length of the tetrahedron is $\sqrt{2}a$. These two helices have the same $H_{\text{ex}}$ energy density of $\frac{8}{9}(Jq^2 - Dq)$, such that their energies are minimized at the same wavevector of $q =$

$2\pi/\lambda = 2D/J$.

However, in terms of the cubic crystalline anisotropy, these two helices actually have different energies. For the $[111]$ helix, $H_{\text{cubic}}^{[111]} = \frac{1}{2}K_c V$, where $V = \frac{1}{3}a^3$ is the volume of the tetrahedron. For the $[001]$ helix, $H_{\text{cubic}}^{[001]} = K_c \int d^3r \left[\frac{1}{2} + \frac{1}{2}\cos^2(2qz + \theta)\right] \geq H_{\text{cubic}}^{[111]}$. The [001] helix always has larger cubic anisotropy energy than the [111] helix. Integrating over the tetrahedron we obtain $H_{\text{cubic}}^{[001]} = \frac{3}{4}K_c V - \frac{K_c}{32q^3}\cos(2qa + 4\theta)[2qa\cos(2qa) - \sin(2qa)]$. In the bulk limit, $H_{\text{cubic}}^{[001]} = \frac{3}{2}H_{\text{cubic}}^{[111]}$. Because the energy scales linearly with the sample volume, at large tetrahedra, the $[111]$ helix is always preferred, which is consistent with the experiment. In the size of interest here, tetrahedra can at least host one period of the helix; therefore, $qa > 2\pi$ and $2qa\cos(2qa) - \sin(2qa) > 0$; then, the [001] helix automatically adjusts its phase to maximize $\cos(2qa + 4\theta)$; therefore, $\theta = -qa/2$.

Surface anisotropy can in principle be present on each surface of tetrahedra, arising from either the dipolar energy or additional surface interaction. Without loss of generality, $H_{\text{surf}} = K_s \int d\sigma (\boldsymbol{M} \cdot \hat{n})^2$ is the dominant lowest order energy term. For the [111] helix, the base plane (111) does not contribute to $H_{\text{surf}}$ because the magnetic moments therein are perpendicular to the normal direction. The contribution from the other three surfaces summed together gives $H_{\text{surf}}^{[111]} = K_s \frac{2a^2}{\sqrt{3}}$. For the $[001]$ helix, all four surfaces contribute to the surface anisotropy energy and $H_{\text{surf}}^{[001]} = K_s \frac{2a^2}{\sqrt{3}} + K_s \frac{2a^2}{\sqrt{3}} \frac{1}{(qa)^2} \cos(qa + 2\theta)\, [qa\cos(qa) - \sin(qa)]$. Taking the value $\theta = -qa/2$ determined from the prevailing cubic anisotropy, $H_{\text{surf}}^{[001]} - H_{\text{surf}}^{[111]} = \frac{2a^2 K_s}{\sqrt{3}} \frac{1}{(qa)^2} [qa\cos(qa) - \sin(qa)] \sim 2K_s a^2/\sqrt{3}qa$ in the large $qa$ limit. For tetrahedra of interest here, this energy difference is approximately equal to or smaller than $0.1K_s a^2$, which is small compared with the other energy terms. Nevertheless, the surface anisotropy still contributes to the formation of the [111] ([001]) helix in the presence of an easy-plane (easy-axis) type $K_s$.

It is difficult to compute the dipolar energy directly; however, a reasonable estimation can be made by examining the total magnetization $\boldsymbol{M}_{\text{total}} = \int \boldsymbol{M} d^3 r$ in the system. For the [111] helix, $\left[\boldsymbol{M}_{total}^{[111]}\right]^2 = (M_s a^3)^2 \frac{3}{8(qa)^6}[2(qa)^4 + 9 + (6(qa)^2 - 9)\cos\frac{2qa}{\sqrt{3}} - 6\sqrt{3}qa\sin\frac{2qa}{\sqrt{3}}]$, whereas for the [001] helix, $\left[\boldsymbol{M}_{total}^{[001]}\right]^2 = (M_s a^3)^2 \frac{16}{(qa)^6}\left(qa\cos\frac{qa}{2} - 2qa\sin\frac{qa}{2}\right)^2$. Because here $qa \gg 1$, $\left[\boldsymbol{M}_{total}^{[111]}\right]^2 \sim \frac{3}{4}(M_s a^3)^2 (qa)^{-2}$ is much greater than $\left[\boldsymbol{M}_{total}^{[001]}\right]^2$. Because the dipolar energy difference $H_d^{[001]} - H_d^{[111]} \sim -\mu_0(\left[\boldsymbol{M}_{total}^{[001]}\right]^2 - \left[\boldsymbol{M}_{total}^{[111]}\right]^2)/V \sim -\frac{27}{4}\mu_0 M_s^2 V (qa)^{-2}$, compared with the cubic anisotropy, small tetrahedra favor the [001] helix instead. Based on this rough estimation, the transition from the [111] to [001] helix occurs at approximately $qa = 2\pi a/\lambda \sim 40$ with $a \sim 450$ nm, which is close to both the simulation result and experimental observation.

## 2. Skyrmionic vortex state

Skyrmionic vortex states can form as either ground or metastable states in tetrahedral nanoparticles. Specifically, a single skyrmionic vortex serves as the ground state in tetrahedra with sizes from 100 to 130 nm. The single- and three-skyrmionic vortex states are present as metastable states in tetrahedra with sizes from 130 to 250 nm. It should be noted that the energy landscape of any 3D spin textures is very complicated because of the comparable energies of competing orders; the metastable magnetic states derived in simulations are quite sensitive to the initial state and the detailed magnetic interactions. It is difficult to classify all the possible states; therefore, here we only focus on the magnetic states that were observed in the experiments.

Although the single-skyrmionic vortex state is mainly driven by chiral geometric frustration, the three-skyrmionic vortex state in particles with size smaller than 200 nm also requires a reduction of the dipole field, i.e., the saturation magnetization, at least in micromagnetic simulations. In real experiments, this is also reasonable because for small particles, the imperfect surfaces could lead to smaller saturation magnetization than the bulk value. To reproduce the 185-nm spin texture observed in the experiment, a reduced saturation magnetization $M_S$ = 192 kA/m was employed.

The surface anisotropy (uniaxial type) was also considered in the simulation. For the helical state, an easy-plane (easy-axis) type surface anisotropy can favor the formation of a helix along the $[111]$ ($[100]$) direction, which is consistent with our analytical analysis. For the skyrmionic state, the surface anisotropy (with the amplitude around the cubic anisotropy) does not substantially affect the phase diagram; however, it does modify the detailed spin textures. To better reproduce the experimental result for a 145-nm tetrahedron, an easy-plane surface type was included in our simulation.

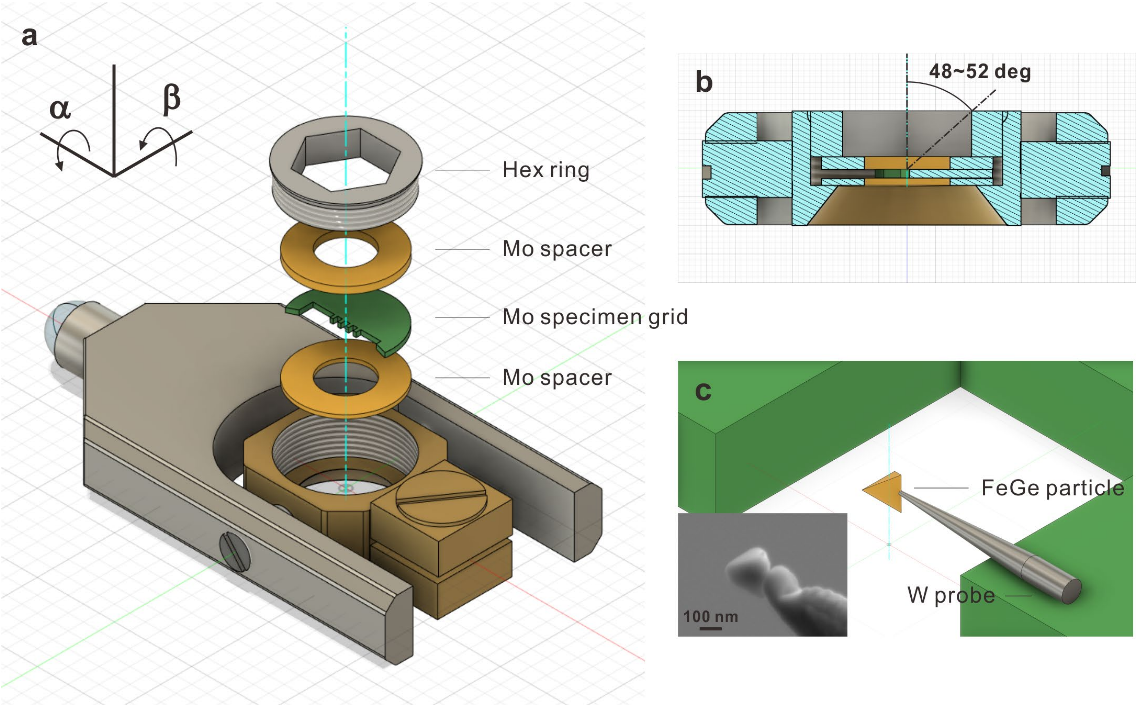

**Supplementary Figure 1 | Sample loading and mechanical configuration for EH observation.** **a**, Schematic illustration of loading the specimen grid into the holder. **b**, Cross-sectional view of (**a**) perpendicular to the α rotation axis. **c**, Magnified view of (**a**) showing a nanoparticle and the supporting tungsten probe. The inset is a typical SEM image captured from the same view angle.

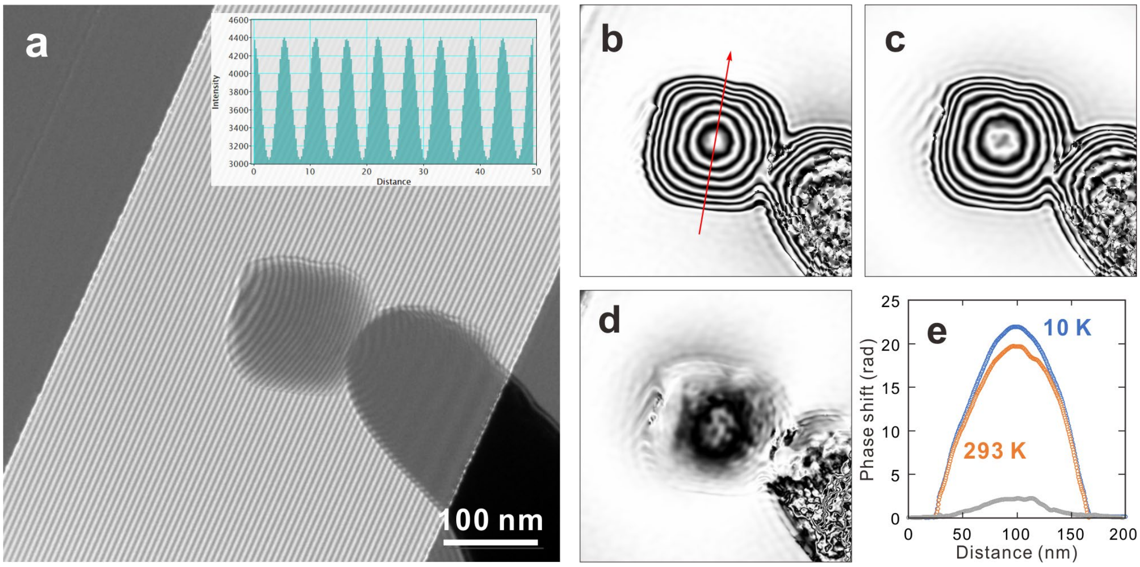

**Supplementary Figure 2 | Hologram acquisition and phase reconstruction procedure.** **a**, Typical hologram recorded at 10 K for a 145-nm tetrahedron. **b**–**d**, Reconstructed phase ($\varphi$) image taken at (**b**) 10 K and (**c**) 293 K in the form of cos($2\varphi$) and (**d**) subtracted one. **e**, Phase shift profiles along the arrow in (**b**) for the images in (**b**), (**c**), and (**d**).

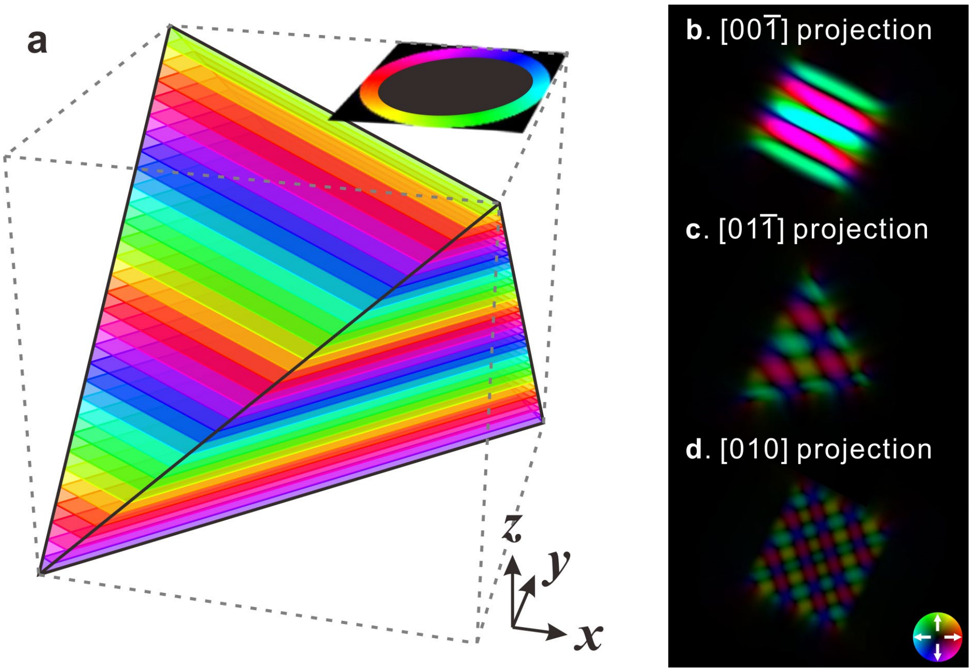

**Supplementary Figure 3 | Protocol and demonstration of the model-based imaging simulations. a**, Schematic of the model for the clockwise helical magnetic structure with $q$ = [001] confined to a 250-nm tetrahedral size. One helical period with a periodic wavelength of 70 nm is divided into twelve discrete thin magnetic phases, which are homogeneously magnetized in the direction normal to the $q$-vector. The magnetization directions of the phases, which are color-coded in line with the inserted color ring, differ from the adjacent ones by 30°. The magnetization of the planes is set to unity. **b**–**d**, Simulated in-plane magnetic flux projections along the (**b**) [00$\bar{1}$], (**c**) [01$\bar{1}$], and (**d**) [010] directions. The inserted color wheel represents the magnetization direction and density as the color hue and brightness, respectively, which are qualitatively comparable among these maps.

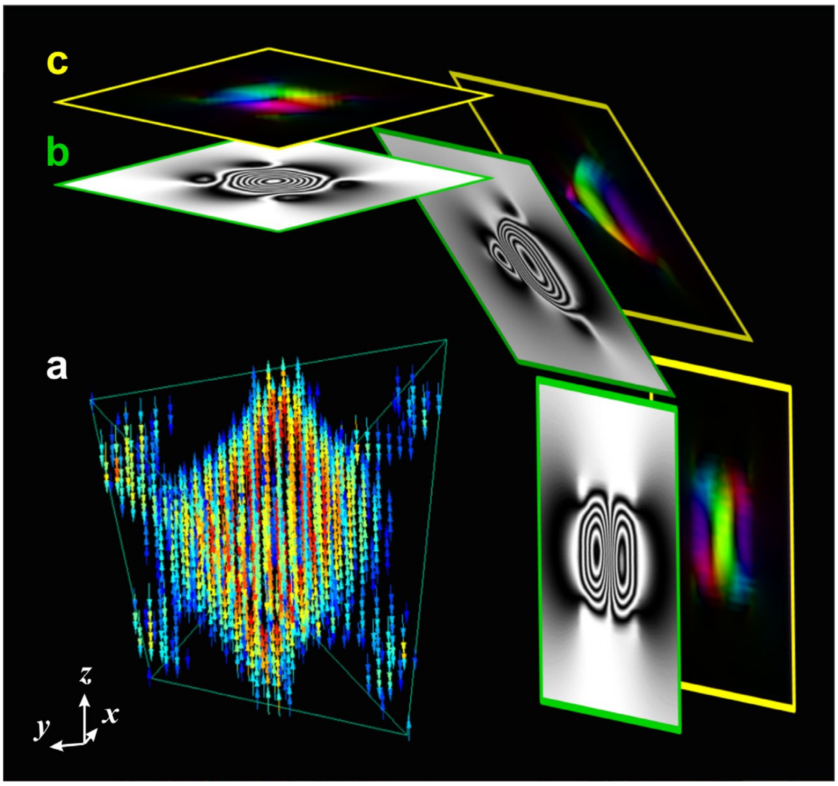

**Supplementary Figure 4 | Protocol to visualize the micromagnetically derived structures as projection maps of the magnetic vector potential as exemplified for a 145-nm nanoparticle.** **a**, Magnetic configurations derived from micromagnetic simulations (only the *z* component is displayed for clear visibility). **b**, Magnetic vector potential $A_{\mathrm{pj}}$ map projected and integrated along the $[00\bar{1}]$, $[01\bar{1}]$, and $[010]$ directions displayed in the form of $\cos(100A_{\mathrm{pj}})$. **c**, Color-coded presentations of the projected magnetic flux distribution where the color hue and brightness represent the in-plane magnetic flux direction and density, respectively.

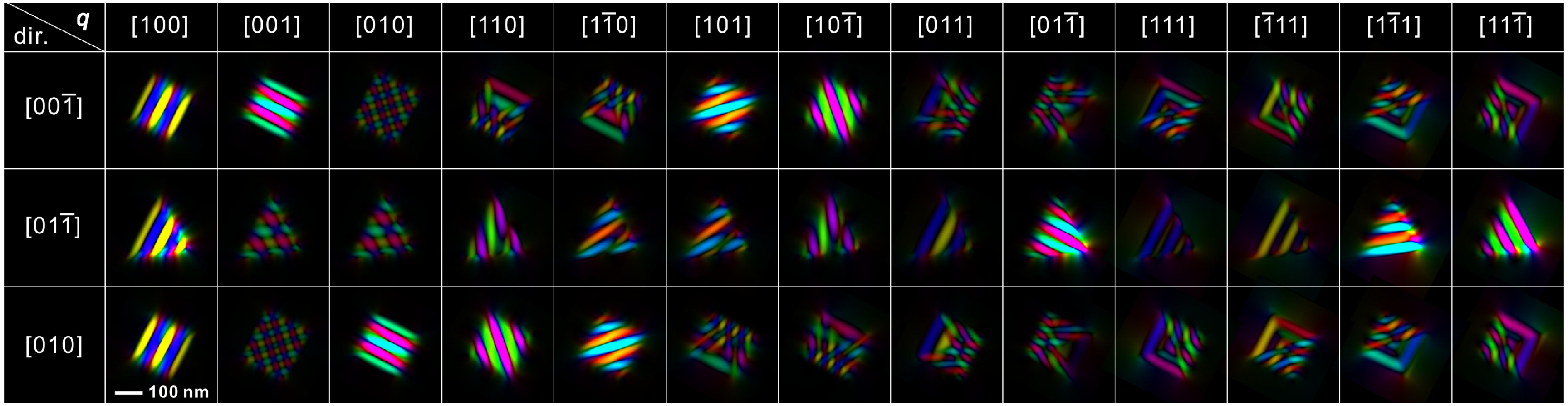

**Supplementary Figure 5 | Suite of $[00\bar{1}]$, $[01\bar{1}]$, and $[010]$ projections of the calculated phase shift distributions for the helimagnetic state with various *q* propagations confined in a 250-nm tetrahedral nanoparticle.**

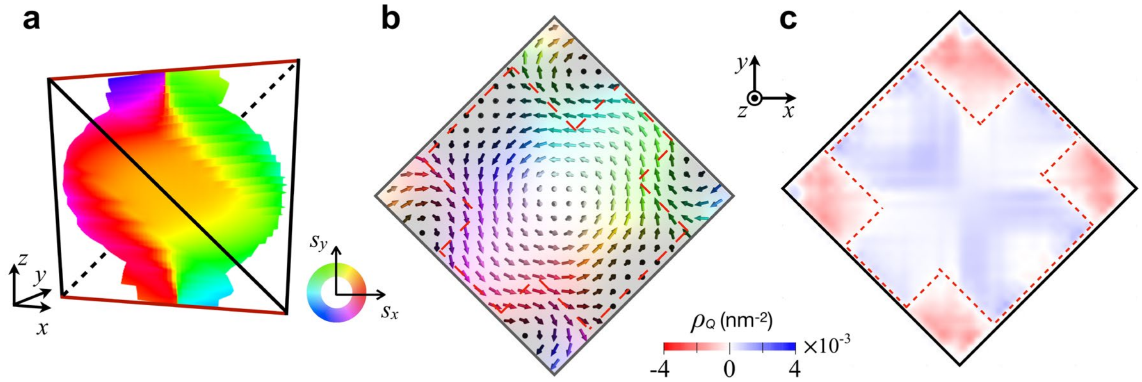

**Supplementary Figure 6 | Single skyrmion configuration in a 145-nm tetrahedron.** **a**, Equi-spin surface for all spins with $S_z = 0$. **b**, *z*-averaged ([001] direction) spin texture of the single skyrmion configuration. **c**, Calculated topological charge density of the magnetic configuration shown in (**b**). The total topological charge within the dashed box is approximately 0.93.

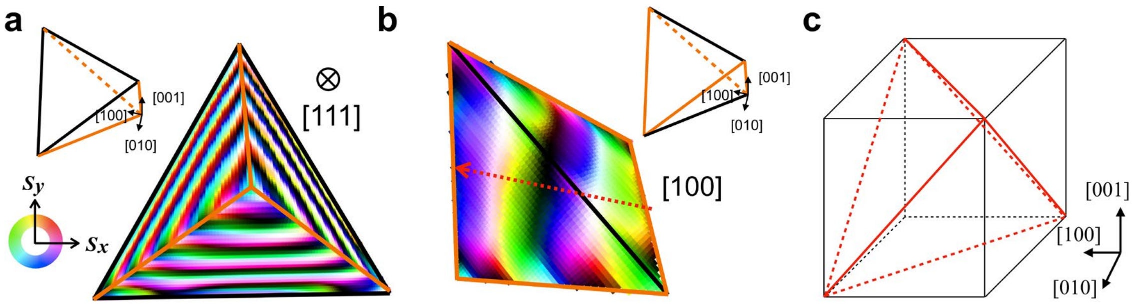

**Supplementary Figure 7 | Transition of the helix direction from [111] to [001]. a**, Top view of helix state along the [111] direction in a 400-nm tetrahedron (corresponding to the orange and black lines in the inset). **b**, Bird's-eye view of helix state along the [100] direction in a 210-nm tetrahedron (corresponding to the orange and black lines in the inset). **c**, Schematic of a tetrahedron embedded within a cube.

## Captions of Supplementary Movies

**Supplementary Movies 1 and 2 | The simulated 3D view of the skyrmionic vortex in a 145-nm tetrahedron.** In-plane (*xy* plane) and out-of-plane (*z* axis) magnetic components are presented in Movies 1 and 2, respectively.